

Multiscale Multimodal Investigation of the Intratissural Biodistribution of Iron Nanotherapeutics with Single Cell Resolution Reveals Co-Localization with Endogenous Iron in Splenic Macrophages

Alice Balfourier, Elena Tsolaki, Laura Heeb, Fabian H. L. Starsich, Daniel Klose, Andreas Boss, Anurag Gupta, Alexander Gogos, and Inge K. Herrmann*

Imaging of iron-based nanoparticles (NPs) remains challenging because of the presence of endogenous iron in tissues that is difficult to distinguish from exogenous iron originating from the NPs. Here, an analytical cascade for characterizing the biodistribution of biomedically relevant iron-based NPs from the organ scale to the cellular and subcellular scales is introduced. The biodistribution on an organ level is assessed by elemental analysis and quantification of magnetic iron by electron paramagnetic resonance, which allowed differentiation of exogenous and endogenous iron. Complementary to these bulk analysis techniques, correlative whole-slide optical and electron microscopy provided spatially resolved insight into the biodistribution of endo- and exogenous iron accumulation in macrophages, with single-cell and single-particle resolution, revealing coaccumulation of iron NPs with endogenous iron in splenic macrophages. Subsequent transmission electron microscopy revealed two types of morphologically distinct iron-containing structures (exogenous nanoparticles and endogenous ferritin) within membrane-bound vesicles in the cytoplasm, hinting at an attempt of splenic macrophages to extract and recycle iron from exogenous nanoparticles. Overall, this strategy enables the distinction of endo- and exogenous iron across scales (from cm to nm, based on the analysis of thousands of cells) and illustrates distribution on organ, cell, and organelle levels.

1. Introduction

Iron-based magnetic nanoparticles (NPs), such as iron oxides or iron carbide NPs, have demonstrated promising potential for medical applications. Such particles have successfully been employed as diagnostic tracers for magnetic resonance (MR)^[1] and magnetic particle imaging (MPI)^[2] for therapeutic purposes (magnetic hyperthermia, targeted drug or gene delivery),^[3,4] in magnetic separation processes (cell isolation, pathogen or toxin removal, or molecular detection)^[5,6] and as magnetic actuators in tissue engineering.^[7] The appealing magnetic properties of iron-based nanoparticles and their high biocompatibility have led to the approval of several iron oxide-based NP formulations for magnetic imaging (e.g., Resovist) and the treatment of iron deficiency (e.g., Venofer or Monofer) by the U.S. Food and Drug Administration and/or European agencies.^[8]

A. Balfourier,^[†] E. Tsolaki, F. H. L. Starsich, A. Gogos, I. K. Herrmann
Nanoparticle Systems Engineering Laboratory
Institute of Energy and Process Engineering (IEPE)
Department of Mechanical and Process Engineering (D-MAVT)
ETH Zurich
8092 Zürich, Switzerland
E-mail: ingeh@ethz.ch



The ORCID identification number(s) for the author(s) of this article can be found under <https://doi.org/10.1002/smt.202201061>.

© 2022 The Authors. Small Methods published by Wiley-VCH GmbH. This is an open access article under the terms of the Creative Commons Attribution-NonCommercial License, which permits use, distribution and reproduction in any medium, provided the original work is properly cited and is not used for commercial purposes.

^[†]Present address: Laboratoire des Biomolécules, Ecole Normale Supérieure, PSL, 75005 Paris, France

A. Balfourier, E. Tsolaki, F. H. L. Starsich, A. Gogos, I. K. Herrmann
Particles-Biology Interactions Laboratory
Department of Materials Meet Life
Swiss Federal Laboratories for Materials Science and Technology (Empa)
9014 St. Gallen, Switzerland

L. Heeb, A. Gupta
Department of Visceral and Transplantation Surgery
and Swiss HPB Center
University Hospital Zurich
8091 Zürich, Switzerland

D. Klose
Department of Chemistry and Applied Biosciences
ETH Zurich
8093 Zürich, Switzerland

A. Boss
Department of Radiology
University Hospital Zurich
8091 Zürich, Switzerland

DOI: 10.1002/smt.202201061

Despite successful transfer from the laboratory to clinics, iron NP-based products suffer from considerable batch-to-batch and product-to-product variability, which has wide-ranging implications, including inconsistent clinical performance.^[9] This variability occurs because the structure–activity relationships remain poorly understood due to the inherent complexity of NP-based drugs^[10,11] and because the assessment of the iron-based NP biodistribution remains challenging, as iron is the most abundant metal present in the body (3 to 4 g for a normal human being in comparison to 2.3 g of zinc, but only 72 mg of copper or 12 mg of manganese).^[12] The distinction between endogenous iron and exogenous iron introduced in the form of NPs is therefore non-trivial, especially not in a spatially resolved manner.

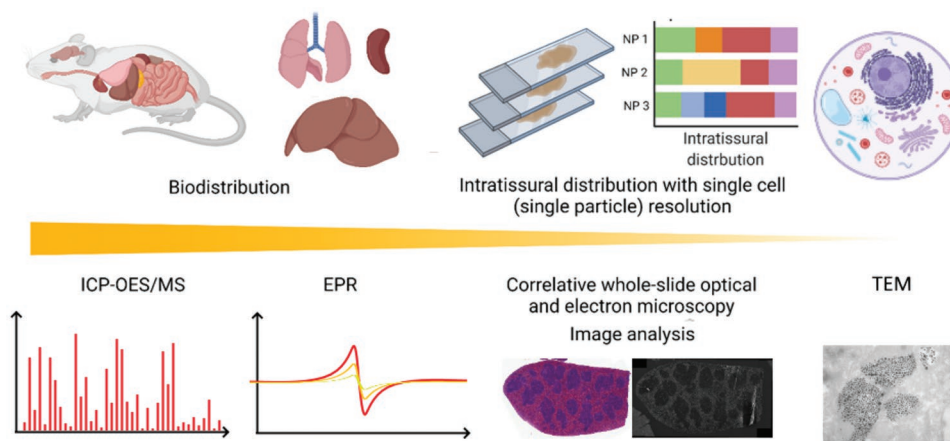
It is well-accepted that intravenously administered inorganic NPs larger than 10 nm accumulate in organs of the reticuloendothelial system (RES), also known as the mononuclear phagocytic system; these macrophage-rich organs include the liver, spleen, and lungs.^[13,14] The biodistribution is strongly dependent on NP size and colloidal stability, and smaller particles may be renally excreted. For larger NPs, histological analyses have indicated that within these organs of the RES, NPs accumulate inside macrophages, such as the Kupffer cells of the liver, the marginal zone and red pulp of the spleen, and the alveolar macrophages of the lungs.^[13,14] Transmission electron microscopy (TEM) investigations have revealed that, at the cellular level, NPs generally accumulate in endosomes and lysosomes, which are acidic organelles responsible for the degradation and recycling of exo- and endogenous compounds.^[13,14] Despite this general knowledge, a comprehensive analysis enabling statistical evaluation of the biodistribution and enabling straightforward unambiguous distinction between endogenous iron and exogenous iron-based NPs and their intratissural distribution has yet to be developed.

Several strategies have been suggested to address this issue, e.g., imaging methods such as magnetic resonance imaging (MRI) have been employed to assess magnetic NP biodistribution in living rodents. This strategy allows the noninvasive detection of label-free NPs in a time-resolved manner. However, MRI is limited by its sensitivity and resolution both in vivo and ex vivo: while subcellular resolution can be achieved in ideal conditions

ex vivo,^[15] in complex biological environments, MRI resolution is limited to 100 μm . Moreover, the inability to quantify the NP biodistribution with sensitivity high enough to detect the entire particle population, or to visualize and distinguish endogenous from exogenous iron limits the applicability of MRI.^[16] MPI may overcome some of these limitations and allows background-free imaging of magnetic NPs with higher temporal resolution, but is not yet widely available and limited to small animal studies.^[16,17] Post-mortem tissue analysis strategies have also been exploited, relying on either the quantification of the magnetic signal by electron paramagnetic resonance (EPR)^[18] and vibrating-sample magnetometry^[19] or the quantification of a tracer based on doping the NPs with another metal or an isotope with low natural abundance.^[20–22] The aforementioned methods enable the quantification of magnetic compounds at the level of entire organs or pieces thereof, but only at the bulk level.

To reach the micrometer scale, which provides access to spatial information with single cell resolution, histopathology remains the gold standard and enables identification of specific cell types inside the tissue. However, the identification and localization of NPs in histological sections typically requires the labeling of the nanoparticles, e.g., with fluorescent probes. Such probes act as surrogate markers to indicate the presence of NPs but suffer from significant drawbacks, including possible detachment of the marker and alteration of the NP characteristics by surface functionalization (e.g., changes in charge and/or hydrophilicity), which potentially affect their biodistribution.^[23,24] Commonly employed techniques, such as Prussian blue staining (also known as Pearl's staining), to detect iron are known to be confounded by the high amount of endogenous iron, resulting in false positive signals that erroneously indicate the presence of NPs, and are thus subject to controversy.^[22] Additionally, such optical microscopy techniques are greatly limited by sensitivity and the optical diffraction limit and do not allow the detection of single particles and small agglomerates.

Here, we propose a set of complementary methods that enable straightforward determination of the biodistribution of iron-based NPs at the organ, cellular, and subcellular levels as well as a straightforward distinction between exogenous iron and the endogenous iron background (**Scheme 1**). At the organ



Scheme 1. Multiscale (from cm to nm) multimodal analytical cascade for the intratissural distribution analysis of inorganic (iron-based) nanoparticles in biological tissues.

scale, elemental analysis by inductively coupled plasma optical emission spectroscopy (ICP-OES) and mass spectrometry (ICP-MS) is employed to measure the amount of iron in the samples. EPR is employed as an orthogonal technique to quantify the amount of exogenous iron. Subsequently, histological sections are investigated to assess the cellular scale based on the correlation of the signal between histologically stained sections for cell type identification (e.g., macrophages) and whole-slide scanning electron microscopy (SEM) in backscattered electron (BSE) mode to allow visualization of metallic NPs directly in the histological samples prepared according to standard procedures. While heavily underused,^[25–27] this visualization method enables direct NP detection and analysis of the intratissural distribution of nonlabeled metallic NPs between different cell types from the single-cell scale to the single-particle scale. This information is not readily available by alternative techniques and typically involves burdensome characterization including mass cytometry^[28,29] or single cell ICP-MS^[30,31] both of which lack spatial information. At the subcellular level, SEM findings can be complemented by conventional TEM with a typically limited field of view to visualize the NPs with ultrastructural context and assess their subcellular localization, state of aggregation, and integrity. Overall, our approach avoids artifacts arising from labels and uses straightforward sample preparation widely available in research laboratories worldwide to provide access to the quantitative intratissue distribution of iron-based nanoparticles with single-cell resolution over large sample areas (and even volumes), yielding statistically meaningful results.

2. Results and Discussion

2.1. Physicochemical Properties of the Nanoparticles

The multiscale multimodal intratissue analysis of iron-based NPs after intravenous injection into the tail veins of

mice was investigated based on two types of biomedically relevant NPs. First, NPs composed of iron carbide (Fe_3C) coated with a few layers of graphene and functionalized with polyethylene glycol (PEG), hereafter named FeC NPs, were considered. These NPs are particularly difficult to identify, as they contain only elements that are highly abundant in the body. FeC NPs have successfully been used for high-performance magnetic separation, hyperthermia applications, and MRI because their saturation magnetization is superior to that of iron oxides.^[32–35] Second, nanoparticle heterostructures made of iron oxide and gold (AuFeOx) stabilized by a thin layer of silica (molar ratio $\text{Au:Fe:Si} \approx 4:1:0.75$) and coated with PEG were investigated. These AuFeOx NPs are readily identifiable based on gold, an element that can be used here as a tracer due to its low abundance in tissue, making the identification of the particles more straightforward. They also unify capabilities for MRI detection and photothermal therapy.^[36]

Scanning transmission electron microscopy (STEM) micrographs of the two types of NPs and elemental analysis by energy dispersive X-ray spectroscopy (EDXS) are displayed in **Figure 1**. Figure 1A–C shows clearly that the three elements Au, Fe, and Si can be detected by EDXS for AuFeOx NPs. The heterostructures contain distinct Au and Fe phases, as can be seen from the differential material contrast and elemental distributions in Figure 1A,B, and are coated with a thin silica shell. Elemental characterization of the carbon content of FeC NPs is more challenging (Figure 1D,E). However, profile analysis performed on NPs clearly evidences the presence of carbon (Figure 1F).

2.2. Analysis of the Biodistribution based on Elemental Analysis and EPR

In order to assess the biodistribution, the two types of NPs were injected into female C57BL/6 mice (8–10 weeks old) via tail vein injection at two doses (200 or 600 μg per mouse corresponding

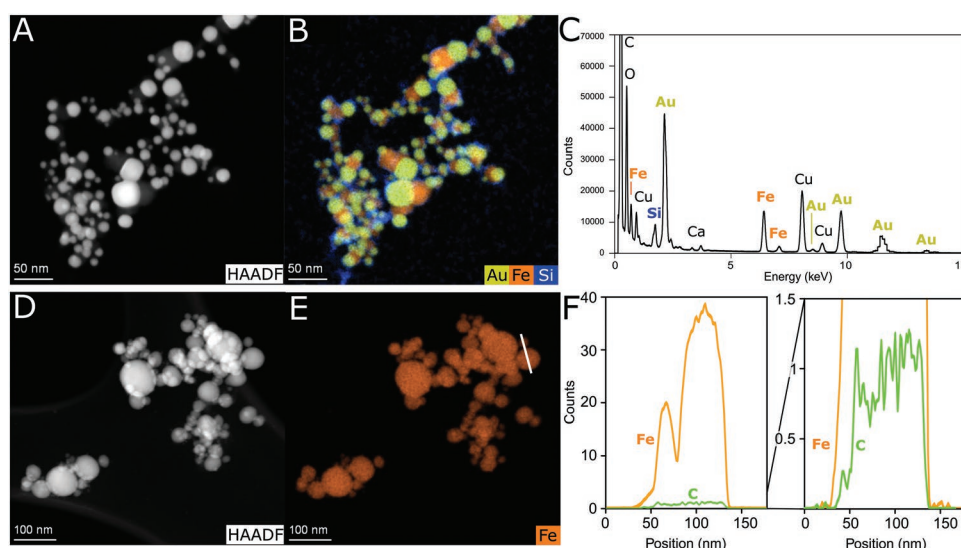


Figure 1. A–C) STEM electron micrograph using A) high angle annular dark field (HAADF) detector and B) elemental mapping of AuFeOx NPs. C) Corresponding EDX spectrum of the AuFeOx NPs. D–F) STEM electron micrograph using D) HAADF detector and E) elemental mapping of FeC NPs. F) EDXS counts of Fe and C along the line indicated in white on panel (E).

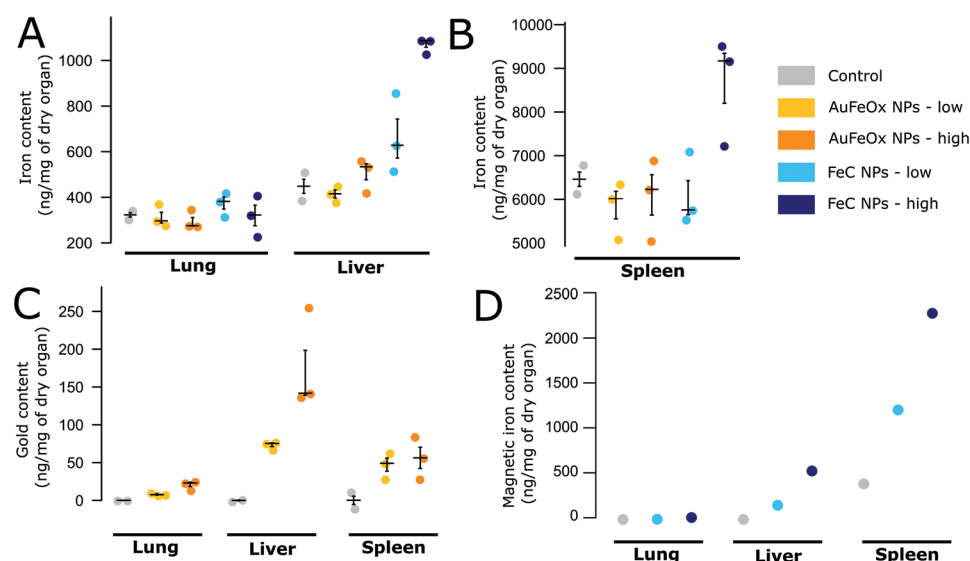


Figure 2. A–C) ICP-OES and ICP-MS analysis of the gold and iron content of lung, liver, and spleen pieces of mice injected with saline (control), AuFeOx NPs, or FeC NPs at different doses. D) EPR analysis of paramagnetic material in lung, liver, and spleen pieces of mice injected with saline (control) or FeC NPs at different doses. Each point represents two pieces of organ from different mice that were pooled together. $N = 3$ per experimental condition. Data show mean \pm standard deviation.

to 8 and 24 mg kg⁻¹ body weight, thereafter named low and high doses, respectively). Mice injected with phosphate-buffered saline as vehicle solution are thereafter referred to as control. One day after the injection, the mice underwent MRI scans before being sacrificed and their organs harvested. Our first objective was to determine the content of exogenous iron in the livers, spleens, and lungs of the mice, which are the organs where the MRI signal indicated the highest presence of iron-containing nanoparticles in previous experiments.^[35] First, ICP-OES and ICP-MS were used to determine the total amount of iron in all the samples and the amount of gold in the AuFeOx NP-exposed samples (Figure 2). As expected, the gold concentration in the control samples was below the detection limit, which enabled the detection of an increase after AuFeOx NP injection based on the gold content in the organs investigated, with a visible dose effect and the highest accumulation in the liver (Figure 2A). In the case of iron, the background was higher due to the presence of endogenous iron, particularly in the spleen, where it reached 6500 ng mg⁻¹ [equivalent to 0.65%] of dry organ mass (Figure 2B,C). Due to the high iron background, the differences in iron load between the control condition and the AuFeOx NPs treatment could not be easily discerned anymore. Similarly, for the FeC NPs, no increase could be seen in the lungs, but an increase in the iron level was visible for both the low and the high dose in the liver. In case of the spleen, the background level was so high that only the high dose showed a noticeable increase. Expectedly, most NPs seemed to accumulate in the liver and the spleen in both cases, interestingly, however, the liver was the main organ of accumulation for AuFeOx NPs, while for the FeC NPs, the main accumulation was observed in the spleen. To overcome the difficult differentiation between endogenous and exogenous iron from FeC NPs, magnetic measurements were performed using EPR (Figure 2D and Figure S1, Supporting Information). Based on EPR, FeC NPs could be detected in all organs,

including the lungs (1.5 ng mg⁻¹ of dry organ for the low dose, 20.5 ng mg⁻¹ for the high dose) with a clear dose effect. These results demonstrated the high accumulation of FeC NPs in the spleen, a lower accumulation in the liver, and a very low accumulation in the lungs, consistent with the ICP-OES/MS data. Excellent agreement was found for the ICP and EPR datasets for the liver samples, as this organ presented both a low endogenous iron level and a pronounced accumulation of FeC NPs (Spearman's rho > 0.85, $p = 0.04$). In the spleen and lung, the high level of endogenous iron in the first case and the low accumulation of NPs in the second did not enable us to obtain a high correlation between the ICP-OES/MS and EPR datasets and illustrates the limitations of the ICP techniques for such cases. Hence, these results strongly support the use of EPR measurements for cases where endogenous and exogenous levels cannot easily be discriminated by ICP.

2.3. Intratissural Distribution of Iron-Based Nanoparticles

Further investigations were, therefore, predominantly focused on the livers and spleens, where most of the nanoparticles accumulated, according to MRI and elemental analysis data. To obtain insights at the cellular level, histological sections were stained with hematoxylin and eosin (H&E staining), to observe the structure of the tissue, or with an anti-F4/80 antibody to visualize macrophages, as they are believed to be the cell type accumulating most of the NPs. Figure 3 shows representative images obtained for a liver exposed to AuFeOx NPs, and a spleen exposed to FeC NPs. Liver tissue shows a rather uniform structure in H&E staining (Figure 3A,B), with macrophages (stained brown) distributed homogeneously in the liver sinusoids (Figure 3D,E), while for the spleen, the red and white pulp can be distinguished based on the pink and purple color in H&E staining (Figure 3G,H).

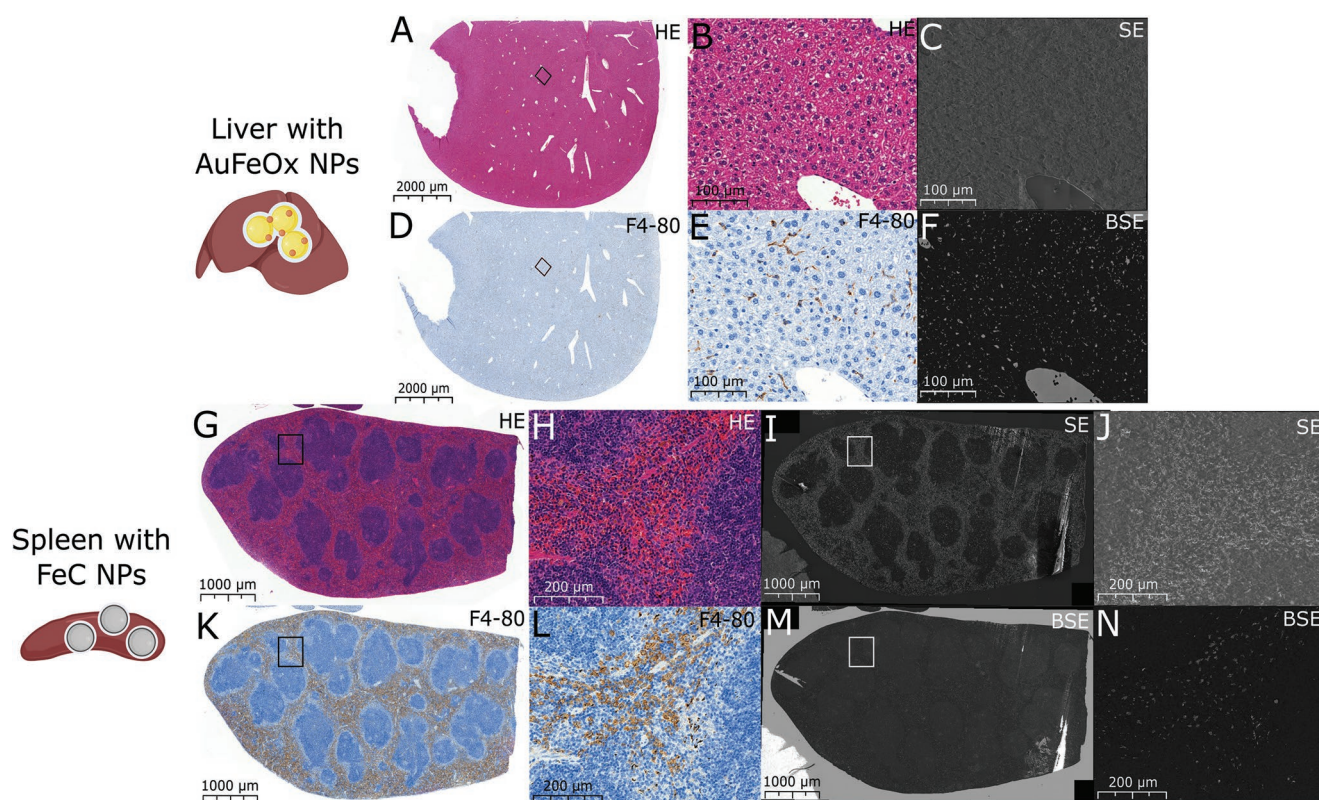


Figure 3. A–F) Whole-slide (WS) optical micrographs of a histological section of the liver of a mouse exposed to a high dose of AuFeOx NPs stained with A,B) H&E or D,E) anti-F4/80. The anti-F4/80 stained section was imaged additionally with WS-SEM in C) SE and F) BSE modes. G–N) WS optical micrograph of a histological section of the spleen of a mouse exposed to a high dose of FeC NPs stained with G,H) H&E or K,L) anti-F4/80. The anti-F4/80 stained section was imaged additionally with WS-SEM in I,J) SE and M,N) BSE modes.

In addition, macrophages in the spleen are nonhomogeneously distributed, most of them were present in the red pulp (Figure 3K,L). Following light microscopy imaging of the standard histological sections, the macrophages-stained sections were observed with an SEM using whole slide scanning mode. Importantly, this procedure can be applied to any histological tissue section mounted on standard microscopy slides, and hence allows high-magnification analysis even of archived samples without the need for any special preparatory steps. WS-SEM imaging was performed using co-registered acquisition in secondary electron (SE) mode, which provides access to the topography of the samples, and BSE mode with sensitivity toward the atomic number, thus yielding a brighter signal in the presence of elements that are heavier than the surrounding organic tissue matrix. The SE signal was consistent with the histological staining, as it underlined the relative homogeneity of the liver (Figure 3C), and the heterogenous structure of the spleen (Figure 3I,J). Regarding the BSE signal (Figure 3F,M,N), bright dot-like signals were observed in both cases, and will be described based on high-magnification analyses (Figure 4).

From the liver observations, comparison between control and NPs-exposed tissues enabled the identification of two types of signals with the BSE mode (Figure 4A–E). First, uniform bright areas were present in all liver samples, including the controls, originating from the microscopy glass slide (Figure 4B, white arrow). Indeed, this background can be attributed to

the glass surface appearing through holes that were present in the histological section due to the porous structure of the liver, as evidenced by the SE image (Figure 4A, white arrow). In the AuFeOx NP treated liver, a second type of high intensity areas, composed of structures with sharp edges and a granular appearance was observed. High-magnification images and EDX spectroscopic analysis (Figure 4C–E) showed that these bright spots originated from both individual and agglomerated nanoscale particles containing iron and gold, suggesting that they were related to AuFeOx NPs (Figure 4G) by comparison to the background signal (Figure 4F). This methodology does not only enable the identification of metal-rich areas in histological sections, as it can also be performed with laser ablation (LA) ICP-MS,^[22] X-ray fluorescence,^[25] or hyperspectral dark-field imaging,^[37] but can also achieve a nanoscale resolution enabling single particle detection (Figure 4E).

For the spleen, the same type of bright granular spots related to the presence of NPs in the tissue was observed (Figure 4J,K), and was associated with the detection of iron (Figure 4M). However, interestingly, all spleen samples, including the spleen tissues of the control mice, also exhibited a low-intensity spongy signal, with heterogenous distribution across the sample (Figure 4L). EDX spectroscopy revealed that these areas are rich in iron, suggesting that the cells that accumulate endogenous iron can be visualized with SEM (Figure 4N). This distinction between endogenous and exogenous iron can only be achieved

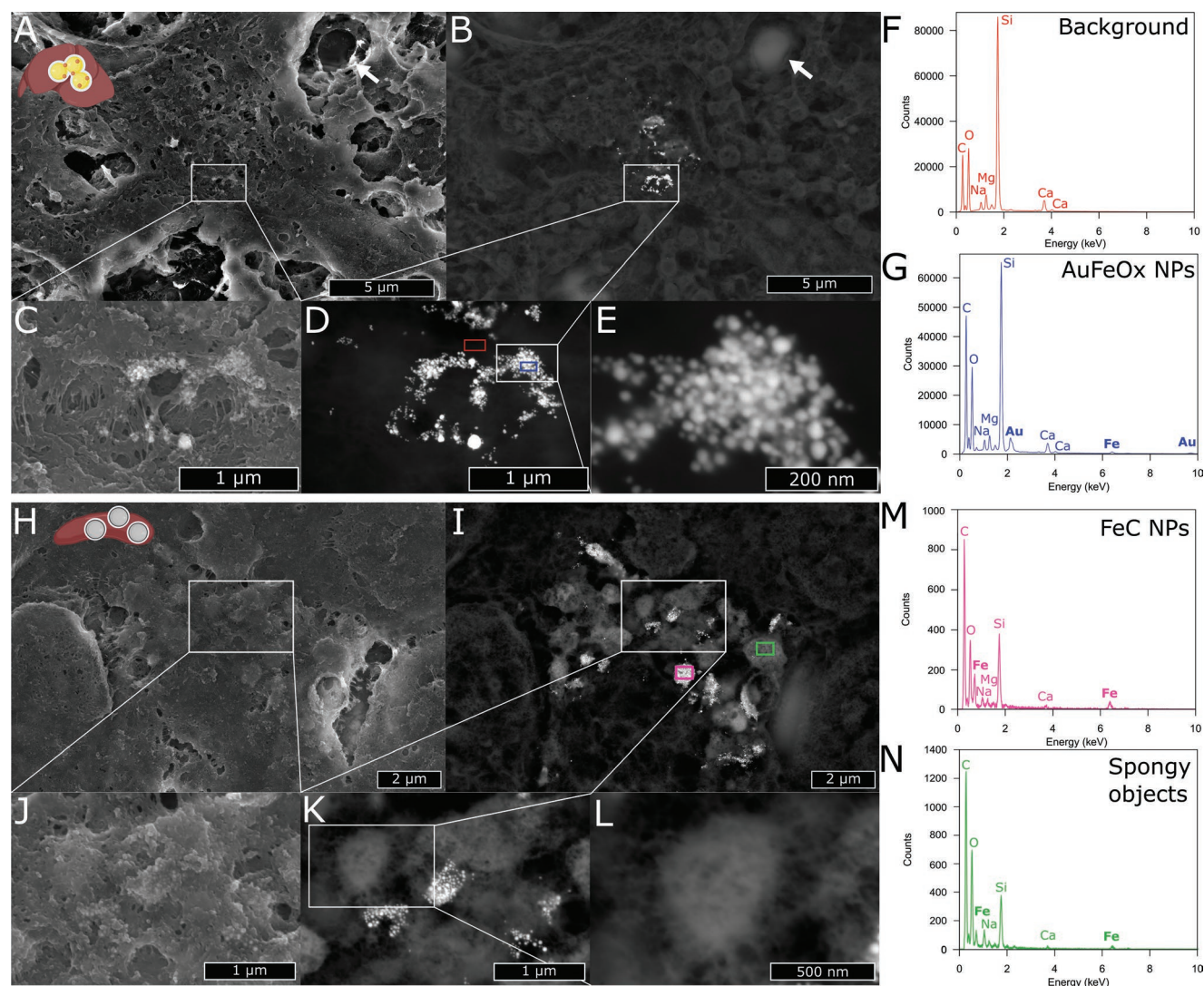


Figure 4. High-magnification scanning electron micrographs acquired using WS-SEM and corresponding EDXS. A–E) Micrographs of a histological section of the liver of a mouse exposed to the high dose of AuFeOx NPs. F,G) Elemental analysis obtained by EDXS on the areas indicated by the F) red and G) blue frames in (D). H–L) Micrographs of a histological section of the spleen of a mouse exposed to the high dose of FeC NPs. M) Elemental analysis obtained by EDXS on the areas indicated by the M) pink and N) green frames in (I). M) These areas contain bright objects meeting the characteristics of exogenously administered NPs or N) on areas containing spongy objects, which are present in both NP-treated and control subjects.

due to the aforementioned nanometric resolution and structural as well as compositional information offered by WS-SEM, showing the particular advantage of this method to discriminate endogenous metals from exogenous metals, as well as the identification of their nanoscale organization.

To correlate histological images with the SEM data, especially the co-localization of NP signals and macrophages, the BSE and macrophage-stained images were overlaid in composite micrographs (following the procedure displayed in Figure S2, Supporting Information). Briefly, the macrophage signals were extracted from the F4/80 stained section (Figure S2A,C, Supporting Information), and the intensity of the BSE signal was converted into color (Figure S2B,D, Supporting Information), ranging from yellow to blue, with blue representing the highest intensity. Both datasets were then merged to create a composite dataset where the two signals

are visible (Figure S2E, Supporting Information). Representative data were assembled to include the original histological images and micrographs, composite pictures, and selected areas for both the liver and the spleen for the control condition (Figure S3, Supporting Information), the organs exposed to the higher dose of AuFeOx NPs (Figure S4, Supporting Information and Figure 5A–H, respectively), and the organs exposed to the higher dose of FeC NPs (Figure 5I–P and Figure S5, Supporting Information, respectively).

In the liver exposed to AuFeOx NPs and in the spleen exposed to FeC NPs, we observed a high correlation between the localization of the NPs and the localization of the macrophages. To quantify this effect, each NP-positive area was classified either as inside a macrophage, neighboring a macrophage (with a typical maximal distance of 2 μm, as sample preparation for WS-SEM can induce small distortion) or excluded from a

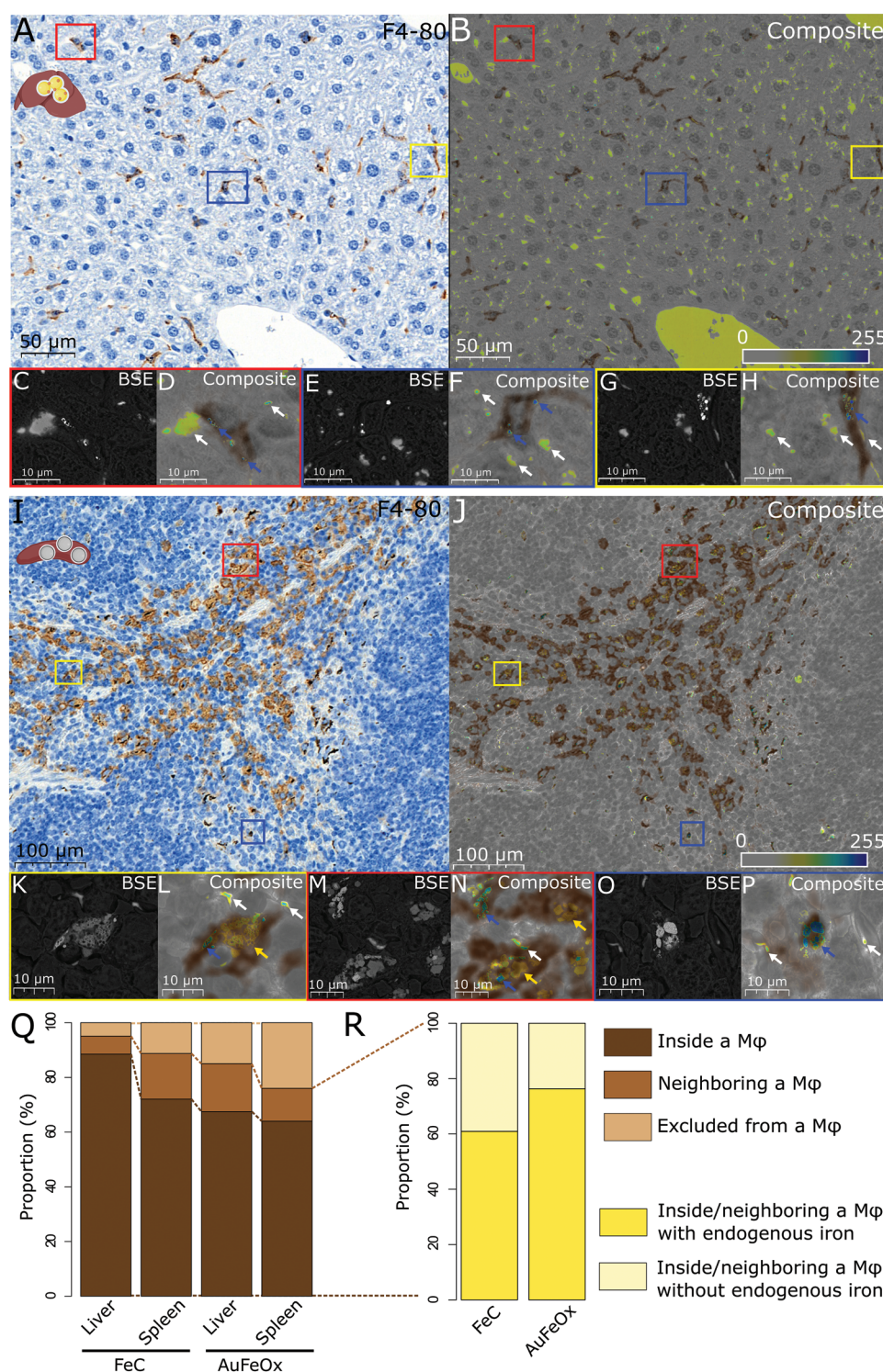


Figure 5. A–H) Superimposition B,D,F,H) of the A) anti-F4/80 antibody-stained section and C,E,G) the BSE signal of the same section of liver containing AuFeOx NPs. The BSE signal is represented as a color range, as indicated in the bottom right corner of the main picture. Blue arrows indicate the AuFeOx NPs, and white arrows indicate the signal from the silica substrate appearing through holes in the samples. I–P) Superimposition J,L,N,P) of the I) anti-F4/80 antibody-stained section and K,M,O) the BSE signal of the same section of spleen after FeC NP exposure. The BSE signal is represented as a color range, as indicated in the bottom right corner of the main picture. The blue arrows indicate the FeC NPs, white arrows indicate the signal from the glass microscopy substrate, and the yellow arrows indicate the signal of endogenous iron. Q) Proportion of NPs detected in macrophages close to macrophages ($d \leq 2 \mu\text{m}$) or far from a macrophage ($d > 2 \mu\text{m}$). Image analysis is based on 61 events for FeC NP-exposed liver, 222 for FeC NP-exposed spleen, 40 for AuFeOx NP-exposed liver, and 50 for AuFeOx NP-exposed spleen samples. R) Proportion of NPs detected in endogenous iron-containing macrophages or macrophages that do not have a signal of endogenous iron. Statistics were made on 197 events for FeC NP-exposed spleen and 38 events for AuFeOx NP-exposed spleen. Mφ stands for macrophage.

macrophage (Figure 5Q). In all NPs-containing samples, 64% and 88% of the NPs-positive areas co-localized with a macrophage for FeC and AuFeOx NPs, respectively, and this proportion increased to 76% and 95%, respectively, when considering NPs inside and neighboring a macrophage. Even if only semiquantitative, this classification suggested a clear trend of NPs capture by the macrophages in these two organs.

In addition, the cells that showed high amounts of endogenous spongy iron also stained positive for macrophage staining, which is consistent with the presumed role of macrophages in the spleen, where they capture aging erythrocytes and recycle the contained iron. Interestingly, not all of the cells that stained positive for F4/80 contained detectable amounts of spongy endogenous iron, indicating the presence of subpopulations of macrophages in the spleen, or a transient nature of the amount of iron contained in the cells at a certain time. A previous study showed that not all macrophages can perform erythrophagocytosis, and only macrophages from the red pulp contribute to endogenous iron recycling, in contrast to macrophages from the marginal zone and metallophilic macrophages.^[38] These latter macrophages still have a phagocytosis activity, but mostly toward pathogens, and represent only around 10% of spleen macrophages.^[39,40] Regarding our two types of iron-based NPs, we observed that 60% to 80% of the macrophages that contained NPs also contained endogenous iron, indicating significant co-accumulation of exogenous with endogenous iron. Further investigation in this direction has the prospect to lead to a better identification of the NPs endocytosis capacities of macrophage subpopulations, and the possible recognition of NPs by macrophages or macrophage subpopulations.

Interestingly, these correlations between optical and electron microscopy datasets also enabled us to study the validity of considering the dark areas appearing in the histological staining as indications for the accumulation of NPs. Figure S6 in the Supporting Information clearly shows the limits of this latter approach. With our correlative imaging approach, however, we have been able to identify, on the one hand, areas that do not appear dark on the histological section but that have a strong BSE signal unambiguously evidencing the presence of nanoparticles (Figure S6A–D, Supporting Information). On the other hand, we also found areas that appeared dark on the section stained for macrophages but that did not present any BSE signal (Figure S6A,B,E–H, Supporting Information). This observation underlines how common approaches based on optical microscopy are insufficient for the detection of label-free NPs, and how our proposed approach can improve the detection of metallic NPs in tissues and enable the study of biodistribution at single cell resolution.

2.4. Subcellular Distribution, Agglomeration State, and Compositional Analysis

While the SEM investigations provide insights into the bio-distribution with single cell resolution and allow extraction of agglomeration characteristics, information on subcellular structures is missing. To contextualize the SEM findings, we acquired TEM data, which additionally provided ultrastructural insights, albeit with a considerably smaller field of view of only a few tens

of microns (Figure 6). The observed agglomeration behavior of the NPs, and the formation of loosely packed agglomerates of AuFeOx NPs (Figure 6C,E,F) or FeC NPs (Figure 6M–Q) with typical diameters in the sub-micron range is in excellent agreement with the SEM observations. Elemental mapping using STEM-EDXS enabled clear identification of the signature elements of AuFeOx NPs (Figure 6G–K and Figure S7A–F, Supporting Information), as well as the iron in FeC NPs (Figure 6R–T and Figure S7G–I, Supporting Information).

In addition to NP signals, dense particles of ≈ 10 –100 nm were observed in the liver, in both the control and NP-exposed samples (Figure 6B and Figure S8A–E, Supporting Information). These particles were highly abundant throughout the samples and showed the characteristics of glycogen particles. Indeed, the liver is the organ where glycogen is stored, and the characteristics of these particles are highly consistent with previous observations of glycogen.^[41] In the spleen, no glycogen was observed, however, accumulation of a different type of dense particle was observed within vesicles in both the NP treated as well as the control samples (Figure 6R,U,V and Figure S8F–I, Supporting Information).

Elemental mapping by EDXS revealed that these particles contained iron, indicating that these structures are ferritin, the protein which stores intracellular endogenous iron. This protein is particularly abundant in the spleen, and appears as 8 nm spherical particles, which is highly consistent with our observations.^[42] Fe stored as ferritin has previously also been detected using electron energy loss spectroscopy (EELS).^[43] However, EELS measurements on tissue sections are considerably more demanding compared to EDXS in terms of sample quality—especially carbon contamination and sample thickness are limiting the applicability of EELS. However, Ferritin-Fe (presumably protein-coordinated Fe, predominantly in the Fe(III)) and Carbide-Fe, which takes on different configurations of Fe_nC_m can be expected to show differences in oxidation state and/or crystallographic structure. Thus, if one could resolve the energy-loss near-edge structure/extended energy-loss fine structure of Ferritin-Fe and nanomaterials-based iron, EELS may offer an interesting approach for chemical (instead of morphological) differentiation. However, TEM alone (and in conjunction with EDXS) also enables the straightforward identification and discrimination of exogenous iron from endogenous iron at the nanoscale, and shows co-accumulation of iron-NPs and endogenous iron in the same vesicular compartments of splenic macrophages. Interestingly, this result hints at a possible attempt of splenic macrophages to extract and recycle iron from exogenous nanoparticles, as suggested for iron oxide NPs elsewhere based on isotopic labeling of NPs.^[21] The NP degradation as well as the recuperation of iron and its efficiency is strongly dependent on particle phase, size, and surface area.^[44]

3. Conclusions

The multiscale multimodal characterization of organs from mice exposed to iron nanotherapeutics by complementary and orthogonal methods revealed the co-accumulation of exogenously administered engineered iron nanotherapeutics with endogenous iron in splenic macrophages. Whole-slide tissue

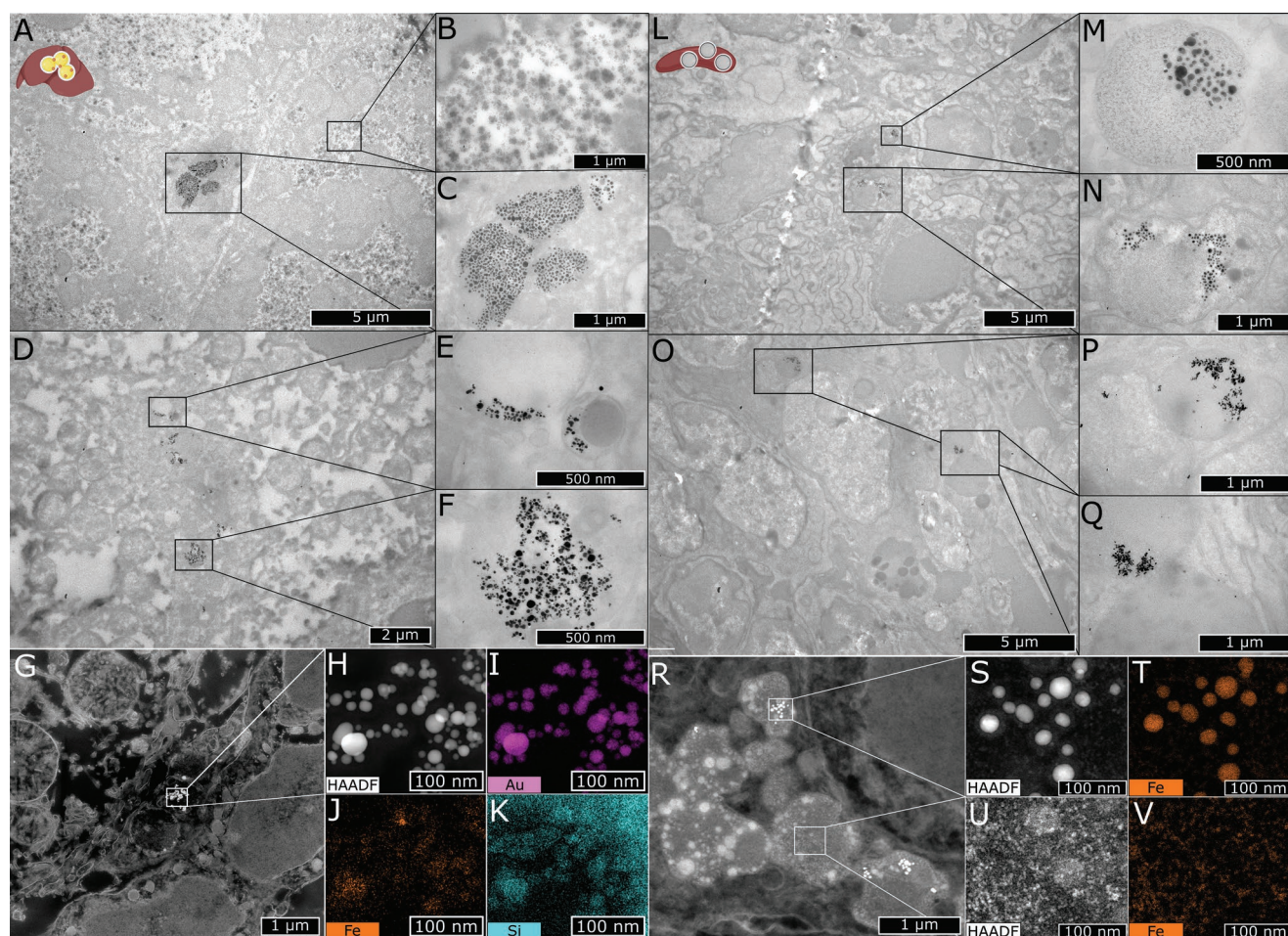


Figure 6. A–F) Transmission electron micrographs of murine liver tissues containing AuFeOx NPs. G–K) and corresponding scanning transmission electron micrographs and elemental mapping by EDXS. L–Q) Transmission electron micrographs of murine spleen tissues containing FeC NPs. R–V) Corresponding scanning transmission electron micrographs and elemental mapping by EDXS. Co-localization of FeC NPs and ferritin can be readily observed in (M), (N), and (R).

analysis gives direct access to intratissural nanoparticle distribution with single cell and even single particle resolution, and allows (semi)quantitative, semi-automated analysis of a large number of cells (several thousand up to even millions of cells) with full histoanatomical context in millimeter large tissue sections, and even volumes. This readily scalable, high-throughput high-resolution imaging approach to tissue analysis is of considerable interest, as it enables the identification of both NPs and specific cell types (based on standard immunohistochemical labeling), without any need to digest and isolate cells, which enables maintaining spatial information as well as true cellular proportion compared to other methods. However, at present, EPR and electron microscopy techniques are only available in specialized research labs. Nonetheless, as standard sample preparation widely employed in research labs and hospitals can be used to prepare and preserve the samples, centralized sample analysis can be envisioned. Low nanoparticle concentrations or highly porous structures of the organs of interest will make the sample analysis more tedious and restrict the use of standard automated image analysis tools. Such samples may need to be deposited on carbon disks instead of standard

histological glass slides for more straightforward analysis. The presented label-free analytical cascade is by no means limited to iron-based particles but provides a straightforward route to investigating the fate of engineered inorganic nanoparticles with single-cell and single-particle resolution using tissues harvested and prepared based on standard tissue procurement procedures. Thus, it can be widely employed in biomedical studies investigating inorganic nanoparticles, or local metal accumulation, as observed with endogenous iron. While this methodology can also be implemented to assess the fate of inorganic nanoparticles over time and monitor their elimination, translocation between organs or biodegradation, the analysis of ionic species and their interaction with metabolic pathways is less straightforward.^[21] However, this strategy bridges an important gap in nanoparticle distribution analysis and opens up a new route to rational material design adjustments based on high-content intratissural biodistribution analyses. Considering metallic compounds more generally, this multimodal characterization method can also be used to determine the localization of endogenous metals and metallic drug accumulation in tissues. It can thus contribute, e.g., to a better understanding

of metal homeostasis, metal overload induced diseases, or the therapeutic and/or toxic action of drugs.

4. Experimental Section

Chemicals: Ethanol $\geq 99.8\%$, (3-aminopropyl)triethoxysilane 99%, L-Cysteine 97%, glutaraldehyde 25%, osmium tetroxide sealed ampules, and epoxy embedding medium kit were purchased from Sigma Aldrich; Ammonia 25% from Honeywell; methoxypoly(ethylene glycol) succinimidyl carbonate from Biochempeg; nitric acid 67% and hydrogen peroxide 30% from VWR; MSAu gold standard, MSFe iron standards, CMS-2 and CCS-6 multielement standards from Inorganic Ventures; sodium cacodylate buffer 0.2 M from Electron Microscopy Sciences were used.

Nanoparticle Synthesis: AuFeOx^[36] and FeC^[32] nanoparticles were synthesized using scalable flame spray pyrolysis. Briefly, iron (and gold) precursors were fed into a spray nozzle, and ignited by an oxygen-methane flame. Nanoparticles were collected in dry state on a filter paper. The as-synthesized nanoparticles were coated with PEG. For this, 10 mg AuFeOx nanoparticles were dispersed in 17.5 mL ethanol using sonication (Sonics Vibra-Cell, Sonics & Materials, Inc., Newtown, CT, USA, 8 kJ, power 90%, pulse on/off 10 s/10 s) for 90 s. Next, 1.25 mL NH₃ was added and the reaction mixture was sonicated for 30 min. Then, 50 μ L (3-aminopropyl)triethoxysilane were added and the reaction mixture was kept at 25 °C for 1 h at 800 rpm. Afterward, the nanoparticles were centrifuged (15 min, 8500 rpm) and washed twice with ethanol and twice with milliQ water and resuspended in 2 mL of borax buffer (final concentration 5 mg mL⁻¹). The amine-functionalized nanoparticles were sonicated for 30 min and 100 mg mPEG-SC (5 k, methoxypoly(ethylene glycol) succinimidyl carbonate) dissolved in 2 mL borax buffer was added and sonicated for 5 min and placed on a shaker for 24 h (25 °C, 800 rpm). Afterward, the functionalized nanoparticles were centrifuged (15 min, 8500 rpm) and washed once in borax buffer and once in milliQ water and stored at 1 mg mL⁻¹ in saline (0.9%). The nonoxidic iron nanoparticles were also functionalized with PEG coating to permit the preparation of stable dispersions of these nanoparticles in water and in biological fluids.

Nanoparticle Administration: The study was approved by the local veterinary office of the canton of Zurich. Nanoparticle injections were performed as previously described.^[35] Female C57BL/6 mice were injected with nanoparticles via tail vein injection at either of the two doses (200 or 600 μ g per mouse) or with equal volumes of vehicle (saline). For each experimental condition, at least three mice were randomly assigned to experimental groups and treated. After termination of the experiment, tissue samples were immediately fixed in formalin and post-fixed in 0.2% glutaraldehyde.

ICP-OES and MS Measurements: Portions of the organs were harvested and weighted. After 2 h of dehydration in pure ethanol, samples were dried under vacuum ($P < 100$ mbar) at 40 °C during 48 to 72 h. Dried samples were weighted again, transferred into Teflon tubes and digested in 1.5 mL of 67% HNO₃. Digestion was performed in a Turbowave unit from MLS GmbH (Germany), following a procedure including temperature and pressure increase to 250 °C and 120 bar, and left for 8 min at these conditions to achieve complete digestion. 0.5 mL of H₂O₂ was then added to the sample, followed by 25 mL of ultrapure water and 25 mL of a 1% L-cysteine solution for Au complexation and stabilization. Depending on the concentration range, the measurements were conducted either on an Agilent 5110 ICP-OES or an Agilent 7900 ICP-MS. For ICP-MS, Au was measured on m/z 197 in He and Fe was measured on m/z 56 in H₂ mode. To correct for non-spectral interferences, an internal standard containing 100 ppb Bi and Rh was mixed online with the sample via a T-piece at a ratio of 1:10. The isotopes ²⁰⁹Bi and ¹⁰³Rh were then used for correction of Au and Fe, respectively. For both, ICP-OES and ICP-MS, calibration standards were always matrix-matched to the same L-cysteine/HNO₃ matrix as the samples.

EPR Spectroscopy: Portion of the organs was harvested, weighted, and lyophilized overnight (Lyophilizer, Christ Alpha 1–2, Martin Christ Gefriertrocknungsanlagen GmbH, Germany) and dried samples were weighted again. The organs were homogenized with a mortar and pestle and filled into 3 mm quartz capillaries (Aachener Quarzglas-Technologie Heinrich GmbH & Co., Germany) to a height of 10–12 mm. A 9-point calibration curve was prepared with dried FeC NP and trehalose as EPR-neutral filling matrix. EPR measurements were performed with an EMX EPR spectrometer (Bruker BioSpin, Rheinstetten, Germany). It was operated in X-band (≈ 9.9 GHz) using a Super-High-Q resonator (Bruker BioSpin) and the first derivative of the reflected microwave power $dW(B)/dB$ was recorded as a function of the external magnetic field B in the range of 10–610 mT. The B field modulation for lock-in amplification had a frequency of 100 kHz and an amplitude of 0.5 mT. The lock-in time constant and conversion time were set to 40 and 327 ms, respectively. The spectra were acquired with a microwave power of 50 mW, while the sample was kept at room temperature via a stream of ambient temperature nitrogen gas through the resonator. The area under the EPR absorption spectrum was calculated by double integration of the spectrum $dW(B)/dB$ and was proportional to the mass of magnetic nanoparticles in the sample. The NP content in the organs was determined using the calibration curve and the weight ratio of wet to dry tissue determined for each sample.

Histology: Samples were paraffin-embedded and sectioned by Sophistolab (Muttentz, Switzerland) and the University Hospital Zurich. Tissue sections were H&E or F4/80 antibody stained, and imaged by optical microscopy with a whole slide scanner (ScopeM, ETH Zurich) using 20X magnification.

Scanning Electron Microscopy: F4-80 antibody stained sections were exposed to xylene to remove paraffin and the glass coverslip, and coated by a 10 nm layer of carbon using a carbon coater (CCU-010, Safematic). Sample observations were made on an FEI Magellan 400 microscope operating at 5 or 10 kV.

Transmission Electron Microscopy: 1 mm³ pieces of samples were washed twice with 0.1 M sodium cacodylate buffer, and stained with 1% osmium tetroxide and 1.5% iron in the sodium cacodylate buffer for 2 h. Samples were then washed three times with water and dehydrated with water:ethanol mixes (successively 75:25, 50:50, 25:70, 5:95), and washed three times with pure ethanol. Cells were then exposed to a 1:1 mix of pure ethanol and Epon for one night, and washed with Epon for 1 hour. Samples were then transferred in fresh Epon and cured at 60 °C for 48 h. Samples were then cut in 70 nm sections that were transferred onto copper grids for observation. Samples were observed on a Hitachi HT 7700 operating at 120 kV (ScopeM, ETH Zurich) or an FEI Talos F200X operating at 200 kV (Scope M, ETH Zurich).

Statistical Analysis: For each experimental condition, at least three mice were randomly assigned to experimental groups, treated and organs harvested and analyzed. Images were treated with Image J software, using Colour Deconvolution 2 and MorphoLibJ plugins^[45,46] yielding semiquantitative data.

Supporting Information

Supporting Information is available from the Wiley Online Library or from the author.

Acknowledgements

The authors acknowledge funding from Innosuisse (grant no. 45085.11P-LS, I.K.H.) and in parts from the Swiss National Science Foundation (Eccellenza grant no. 181290, I.K.H.). The authors also acknowledge funding from the Sassella Stiftung and Yvonne Jacob Stiftung (A. Gupta). The authors thank the ETH Center for Microscopy (ScopeM) and the University of Zurich Microscopy Center for their support and for access to their microscopes.

Conflict of Interest

The authors declare no conflict of interest.

Author Contributions

A. Balfourier contributed to study design, performed the experiments, and drafted the manuscript. E.T. performed the whole slide electron microscopy analysis. L.H. performed the animal experiments together with A. Boss and A. Gupta. F.H.L. synthesized the nanoparticles. D.K. performed the EPR measurements, A. Gogos performed the elemental analysis. I.K.H. conceived the study and co-wrote the manuscript. All authors contributed to data analysis, interpretation, edited, and approved the manuscript.

Data Availability Statement

The data that support the findings of this study are available from the corresponding author upon reasonable request.

Keywords

biodistribution, correlative microscopy, endo/exogenous iron distinction, nanoparticle fate

Received: August 16, 2022

Revised: December 2, 2022

Published online: December 26, 2022

- [1] Z. Shen, A. Wu, X. Chen, *Mol. Pharmaceutics* **2017**, *14*, 1352.
- [2] N. Talebloo, M. Gudi, N. Robertson, P. Wang, *J. Magn. Reson. Imaging* **2020**, *51*, 1659.
- [3] K. El-Boubbou, *Nanomedicine* **2018**, *13*, 929.
- [4] F. Soetaert, P. Korangath, D. Serantes, S. Fiering, R. Ivkov, *Adv. Drug Delivery Rev.* **2020**, *163–164*, 65.
- [5] I. K. Herrmann, A. A. Schlegel, R. Graf, W. J. Stark, B. Beck-Schimmer, *J. Nanobiotechnol.* **2015**, *13*, 49.
- [6] M. Iranmanesh, J. Hulliger, *Chem. Soc. Rev.* **2017**, *46*, 5925.
- [7] R. P. Friedrich, I. Cicha, C. Alexiou, *Nanomaterials* **2021**, *11*, 2337.
- [8] A. C. Anselmo, S. Mitragotri, *Bioeng. Transl. Med.* **2019**, *4*, e10143.
- [9] D. R. Baer, *Front. Chem.* **2018**, *6*, 145.
- [10] D. A. Winkler, *Toxicol. Appl. Pharmacol.* **2016**, *299*, 96.
- [11] A. Frtús, B. Smolková, M. Uzhytychak, M. Lunova, M. Jirsa, Š. Kubinová, A. Dejneka, O. Lunov, *J. Controlled Release* **2020**, *328*, 59.
- [12] *Metallomics* (Ed: M. A. Z. Arruda), Advances in Experimental Medicine and Biology, Vol. 1055, Springer International Publishing, Cham **2018**.
- [13] H. Arami, A. Khandhar, D. Liggitt, K. M. Krishnan, *Chem. Soc. Rev.* **2015**, *44*, 8576.
- [14] J. P. M. Almeida, A. L. Chen, A. Foster, R. Drezek, *Nanomedicine* **2011**, *6*, 815.
- [15] H. C. Davis, P. Ramesh, A. Bhatnagar, A. Lee-Gosselin, J. F. Barry, D. R. Glenn, R. L. Walsworth, M. G. Shapiro, *Nat. Commun.* **2018**, *9*, 131.
- [16] H. Paysen, N. Loewa, K. Weber, O. Kosch, J. Wells, T. Schaeffter, F. Wiekhorst, *J. Magn. Magn. Mater.* **2019**, *475*, 382.
- [17] A. Neumann, K. Gräfe, A. von Gladiss, M. Ahlberg, A. Behrends, X. Chen, J. Schumacher, Y. Blancke Soares, T. Friedrich, H. Wei, A. Malhorta, E. Aderhold, A. C. Bakenecker, K. Lüttke-Buzug, T. M. Buzug, *J. Magn. Magn. Mater.* **2022**, *550*, 169037.
- [18] B. Chertok, A. J. Cole, A. E. David, V. C. Yang, *Mol. Pharmaceutics* **2010**, *7*, 375.
- [19] M. K. Jaiswal, M. Gogoi, H. D. Sarma, R. Banerjee, D. Bahadur, *Biomater. Sci.* **2014**, *2*, 370.
- [20] I. K. Herrmann, B. Beck-Schimmer, C. M. Schumacher, S. Gschwind, A. Kaech, U. Ziegler, P.-A. Clavien, D. Günther, W. J. Stark, R. Graf, A. A. Schlegel, *Nanomedicine* **2016**, *11*, 783.
- [21] J. Volatron, *Cycle de vie de nanoparticules dans l'organisme : biotransformations et biodégradation*, Sorbonne Paris Cité **2018**.
- [22] C. Scharlach, L. Müller, S. Wagner, Y. Kobayashi, H. Kratz, M. Ebert, N. Jakubowski, E. Schellenberger, *J. Biomed. Nanotechnol.* **2016**, *12*, 1001.
- [23] W. G. Kreyling, A. M. Abdelmonem, Z. Ali, F. Alves, M. Geiser, N. Haberl, R. Hartmann, S. Hirn, D. J. de Aberasturi, K. Kantner, G. Khadem-Saba, J.-M. Montenegro, J. Rejman, T. Rojo, I. R. de Larramendi, R. Ufartes, A. Wenk, W. J. Parak, *Nat. Nanotechnol.* **2015**, *10*, 619.
- [24] M. Xu, M. G. Soliman, X. Sun, B. Pelaz, N. Feliu, W. J. Parak, S. Liu, *ACS Nano* **2018**, *12*, 10104.
- [25] M. T. Matter, J. Li, I. Lese, C. Schreiner, L. Bernard, O. Scholder, J. Hubeli, K. Kevend, E. Tsolaki, E. Bertero, S. Bertazzo, R. Zboray, R. Olariu, M. A. Constantinescu, R. Figi, I. K. Herrmann, *Adv. Sci.* **2020**, *7*, 2000912.
- [26] H. A. Lowers, G. N. Breit, M. Strand, R. M. Pillers, G. P. Meeker, T. I. Todorov, G. S. Plumlee, R. E. Wolf, M. Robinson, J. Parr, R. Miller, S. Groshong, F. Green, C. Rose, *Toxicol. Mech. Methods* **2018**, *28*, 475.
- [27] J. Fleddermann, J. Susewind, H. Peuschel, M. Koch, I. Tavernaro, A. Kraegleloh, *Int. J. Nanomed.* **2019**, *14*, 1411.
- [28] Y.-S. S. Yang, P. U. Atukorale, K. D. Moynihan, A. Bekdemir, K. Rakhra, L. Tang, F. Stellacci, D. J. Irvine, *Nat. Commun.* **2017**, *8*, 14069.
- [29] M. K. Ha, S. J. Kwon, J. Choi, N. T. Nguyen, J. Song, Y. Lee, Y. Kim, I. Shin, J. Nam, T. H. Yoon, *Small* **2020**, *16*, 1907674.
- [30] R. C. Merrifield, C. Stephan, J. R. Lead, *Environ. Sci. Technol.* **2018**, *52*, 2271.
- [31] X. Wei, D.-H. Zheng, Y. Cai, R. Jiang, M.-L. Chen, T. Yang, Z.-R. Xu, Y.-L. Yu, J.-H. Wang, *Anal. Chem.* **2018**, *90*, 14543.
- [32] I. K. Herrmann, M. Urner, F. M. Koehler, M. Hasler, B. Roth-Z'Graggen, R. N. Grass, U. Ziegler, B. Beck-Schimmer, W. J. Stark, *Small* **2010**, *6*, 1388.
- [33] I. K. Herrmann, R. N. Grass, W. J. Stark, *Nanomedicine* **2009**, *4*, 787.
- [34] A. Gangwar, S. S. Varghese, S. S. Meena, C. L. Prajapat, N. Gupta, N. K. Prasad, *J. Magn. Magn. Mater.* **2019**, *481*, 251.
- [35] A. Boss, L. Heeb, D. Vats, F. H. L. Starsich, A. Balfourier, I. K. Herrmann, A. Gupta, *NMR Biomed.* **2022**, *35*, e4690.
- [36] G. A. Sotiriou, F. Starsich, A. Dasargyri, M. C. Wurnig, F. Krumeich, A. Boss, J.-C. Leroux, S. E. Pratsinis, *Adv. Funct. Mater.* **2014**, *24*, 2818.
- [37] E. D. SoRelle, O. Liba, J. L. Campbell, R. Dalal, C. L. Zavaleta, A. de la Zerda, *Elife* **2016**, *5*, e16352.
- [38] Z. Bian, L. Shi, Y.-L. Guo, Z. Lv, C. Tang, S. Niu, A. Tremblay, M. Venkataramani, C. Culpepper, L. Li, Z. Zhou, A. Mansour, Y. Zhang, A. Gewirtz, K. Kidder, K. Zen, Y. Liu, *Proc. Natl. Acad. Sci. USA* **2016**, *113*, E5434.
- [39] H. Borges da Silva, R. Fonseca, R. M. Pereira, A. dos A. Cassado, J. M. Álvarez, M. R. D'Império Lima, *Front. Immunol.* **2015**, *6*, 480.
- [40] S. Fujiyama, C. Nakahashi-Oda, F. Abe, Y. Wang, K. Sato, A. Shibuya, *Int. Immunol.* **2019**, *31*, 51.

- [41] J. P. Revel, *J. Histochem. Cytochem.* **1964**, 12, 104.
- [42] N. Jian, M. Dowle, R. D. Horniblow, C. Tselepis, R. E. Palmer, *Nanotechnology* **2016**, 27, 46LT02.
- [43] M. Fukunaga, T.-Q. Li, P. van Gelderen, J. A. de Zwart, K. Shmueli, B. Yao, J. Lee, D. Maric, M. A. Aronova, G. Zhang, R. D. Leapman, J. F. Schenck, H. Merkle, J. H. Duyn, *Proc. Natl. Acad. Sci. USA* **2010**, 107, 3834.
- [44] E. Casals, G. Casals, V. Puntos, J. M. Rosenholm, in *Theranostic Bionanomaterials* (Eds: W. Cui, X. Zhao), Elsevier, New York **2019**, pp. 3–26.
- [45] G. Landini, G. Martinelli, F. Piccinini, *Bioinformatics* **2021**, 37, 1485.
- [46] D. Legland, I. Arganda-Carreras, P. Andrey, *Bioinformatics* **2016**, 32, 3532.